



Versatile setup for high-quality rephasing, non-rephasing, and double quantum 2D electronic spectroscopy

LUCA BOLZONELLO, ANDREA VOLPATO, ELENA MENEGHIN, AND ELISABETTA COLLINI*

Department of Chemical Science, University of Padova, via Marzolo 1, Padova 35131, Italy

*Corresponding author: elisabetta.collini@unipd.it

Received 24 February 2017; revised 13 April 2017; accepted 1 May 2017; posted 3 May 2017 (Doc. ID 287258); published 23 May 2017

Two-dimensional electronic spectroscopy based on passive phase stabilization methods is now well known and widely employed worldwide. In the most recent fully non-collinear implementations, a great phase stability is often achieved at the expense of the independent control over the pulse timings, limiting the full potential of the technique. Here we propose several modifications in the experiment geometry, calibration procedures, and data acquisition and processing routines. The setup is easily tunable to record different phase-matching directions, such as rephasing, non-rephasing and double quantum signals, still maintaining high levels of phase control and phase stability. The performances of the proposed setup are exemplified by measures on the standard dye zinc phthalocyanine and porphyrin J-aggregates.

Published by The Optical Society under the terms of the [Creative Commons Attribution 4.0 License](https://creativecommons.org/licenses/by/4.0/). Further distribution of this work must maintain attribution to the author(s) and the published article's title, journal citation, and DOI.

OCIS codes: (300.6240) Spectroscopy, coherent transient; (300.6530) Spectroscopy, ultrafast; (300.6290) Spectroscopy, four-wave mixing; (300.6300) Spectroscopy, Fourier transforms.

<https://doi.org/10.1364/JOSAB.34.001223>

1. INTRODUCTION

Two-dimensional electronic spectroscopy (2DES) is a third-order non-linear technique which is successfully spreading in the latest years thanks to its capability of unraveling fine details of the ultrafast dynamics of the systems under investigation [1–3]. 2DES is based on the interaction of three ultrafast laser pulses with an optical sample. The experiment consists of probing the resulting third-order optical polarization as a function of the time delays between the three different interactions. A typical pulse sequence with the definition of the time variables is reported in Fig. 1(a). The capability of 2DES to scan independently the three time delays between pairs of pulses allows disentangling overlapped signals and unraveling correlations between different transitions. Suitable pulse sequence definition allows indeed the access to rephasing (R), non-rephasing (NR), and double quantum (2Q) signals, each one providing different and complementary information [4,5]. This flexibility enables investigation of molecular systems with previously unavailable detail; for example, molecular couplings and energy relaxation pathways can be directly followed and the temporal evolution of both coherent and non-coherent processes can be characterized.

The first 2DES spectrometer [6] was based on a fully non-collinear BOXCAR geometry. Since then, other geometries

have been proposed [7–11] and recently reviewed by Fuller and Ogilvie [12]. The fully non-collinear geometry remains, however, the most adopted configuration and most efforts are still being paid in the development of new technological solutions to overcome the well-known issues and to improve the quality of the data.

One of the major sources of signal degradation in fully non-collinear setups is the lack of phase stability, i.e., the capability to keep constant the phase difference between pairs of optical pulses for a given time delay [13].

Many different approaches have been used to increase the phase stability in fully non-collinear 2DES experiments, including active [14] and passive phase stabilization methods, through diffractive optics (DO) [15,16], pulse shaping [17] and, more in general, particular geometries that allow the phase-locking of specific pulse pairs [18,19]. These last methods, in particular, achieve a great phase stability working in a full optical rotating frame, but they require coupling the motion of pairs of pulses, partially losing the independent control of timings. Therefore, a better phase stability is obtained at the cost of a less versatile setup, unable to exploit the full potential of 2DES.

Here we report an experimental scheme for a fully non-collinear 2DES whose optical layout has been specifically designed to provide full independent control over all the time

intervals allowing an easy retrieval of all the different phase-matching signals (R, NR, and 2Q), still maintaining excellent reliability and particularly high short- and long-term phase stability.

Experimental data recorded for a tetrahydrofuran (THF) solution of zinc phthalocyanine (ZnPc) are used to elucidate the crucial features of the proposed setup and of the corresponding data processing routines. The full potential of the described approach is exemplified through the characterization of the full 2D response of solutions of J-aggregates of the diacid form of the water-soluble tetra-(*p* sulphonato)-phenylporphyrin (H_2 TPPS).

2. OPTICAL LAYOUT AND PULSE SEQUENCE

The experimental setup is illustrated in Fig. 1. The scheme is inspired to the BOXCARS geometry proposed by Nemeth *et al.* [16]. A Coherent Libra laser system generates a continuous pulse train centered at 800 nm with a repetition rate of 3 KHz. The central wavelength of laser pulses is converted in the visible range using a commercial NOPA (Light Conversion TOPAS White).

Before entering the optical setup, the pulses from the NOPA pass through a stage of pulse shaping [with an acousto-optic programmable dispersive filter (AOPDF), Fastlite Dazzler] and

prisms compression to maximize the time resolution of the experiment and to guarantee full control over the phase of the different frequency components in the broadband pulse. A detailed description of the pulse shaping stage is reported in Section 3.

Four identical beams in BOXCARS geometry are obtained focusing the incoming beam into a 2D-DO element with spherical mirror SM3. The DO is a 2 mm thick phase mask that is etched in a 2D cross-hatched pattern where the width and the depth of the features are optimized for first-order diffraction of the incident wavelength. Since the diffraction properties of the DO are wavelength dependent, different suitably optimized DOs could be necessary to achieve maximum performances in different spectral ranges. The four first-order diffraction beams, each about 10% of the input power, are arranged in the BOXCARS configuration, as depicted in Fig. 1(b). The outgoing divergent beams are collimated and parallelized by a donut-shaped spherical mirror (DSM1), with the same focal length of the focusing mirror SM3 (500 mm).

The main advantage of using a 2D-DO is the more easy retrieval of the BOXCARS phase-matching conditions, naturally emerging from the 2D diffraction pattern, whereas the use of a 1D-DO requires an additional preliminary step of beam splitting through conventional optics and the subsequent

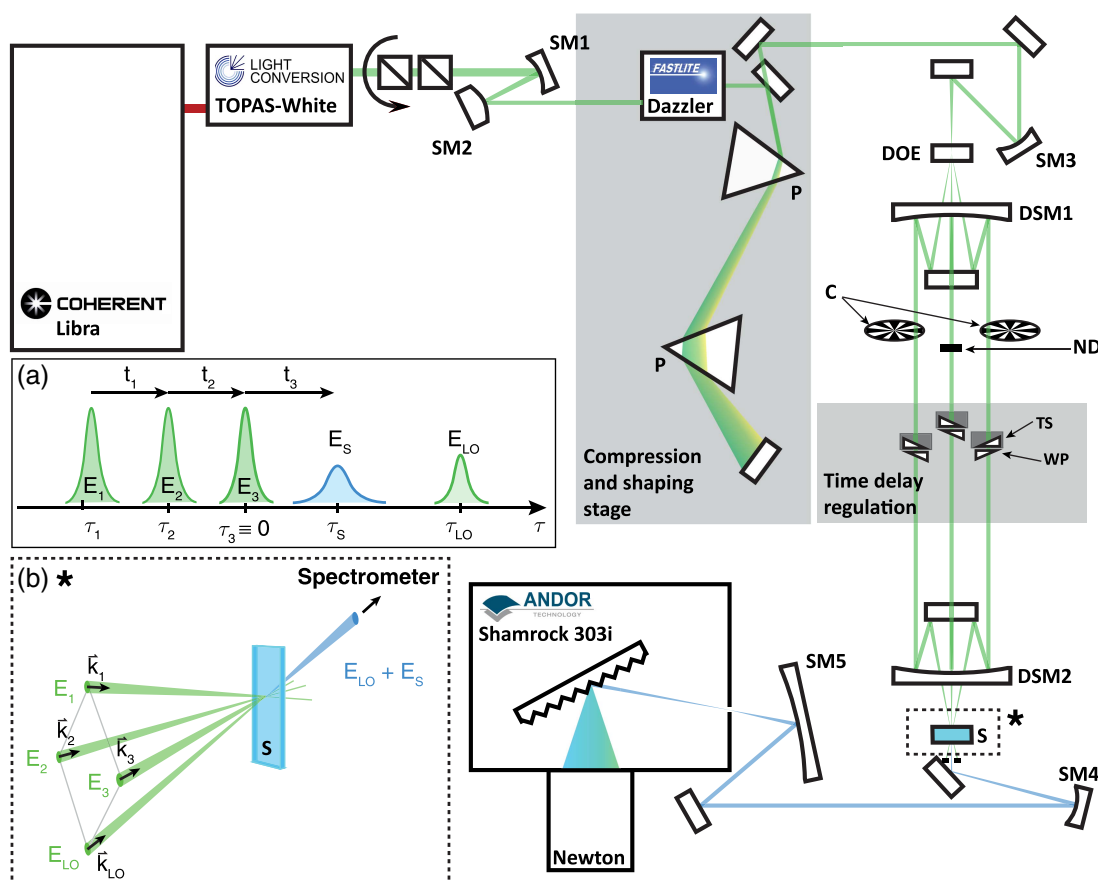


Fig. 1. Schematic 2DES setup. Abbreviations: SM, spherical mirror; P, prism; DO, bi-dimensional diffractive optical element; DSM, donut spherical mirror; C, chopper; ND, neutral density filter; WP, wedge pair; TS, translational stage; S, sample. Panel (a) describes the pulse sequence and the time intervals definition in a 2DES rephasing experiment. Panel (b) reports a schematic representation of BOXCARS geometry, where E_i are the three interacting fields, \mathbf{k}_i are the wave vectors, and E_{LO} is the fourth pulse used for heterodyne detection.

alignment of pairs of beams to form a square. A drawback of this configuration is that the time delays between pulses can be introduced conveniently only through antiparallel wedge pairs (WP). Typically, a 1° fused silica wedge pair is employed, which is capable of providing a time delay of the order of hundreds of femtoseconds. This is enough for t_1 but it can be limiting for t_2 , where one might be interested in observing phenomena with longer characteristic time scales (of the order of picoseconds). In the proposed setup this complication is overcome through the use of 4° CaF₂ 25 mm long wedges, providing time delays up to 2 ps. Instead of fused silica, the choice of CaF₂ is more suitable since it induces less phase distortion in broadband pulses. Such wedges require anyway a more careful calibration procedure, as described in Section 4. The insertion of wedges in the beam path could produce small deviations in the beam propagation. This is detrimental for the fulfillment of the phase-matching conditions, because any deviation, even of a small angle, on the direction of one of the beams can produce artifacts in the collected signal [20]. To correct these possible deviations, the geometry and spatial propagation of the beams is controlled with a charge-coupled device (CCD) camera, allowing the optimization of the wedges orientation.

One wedge from each pair is mounted on a computer-controlled linear delay stage (Aerotech Ant 95), whose position has to be accurately controlled to guarantee repeatability and precision of the time delays between pulses (in our setup the repeatability is of about 0.07 fs and the phase stability is higher than $\pi/20$). The fourth pulse is used as a local oscillator (LO) and its power is conveniently attenuated with a graduated neutral filter in order to maximize the heterodyne signal. Its temporal position is kept fixed during the 2DES experiment and thus it can be conveniently set as reference time for the definition of the time delays.

This configuration enables us to scan independently all the different time delays of the three exciting beams, easily obtaining the R, NR, and 2Q signals simply designing the correct pulse sequence. We found that the most suitable configuration consists of fixing the time position of the pulse generating the third interaction with the system, i.e., E_3 for the R and NR signals and E_1 for the 2Q signal. The other two pulses are scanned accordingly to construct the full 2DES spectra. This choice has the major benefit of guaranteeing a phase-locking relation between E_3 (E_1) and the LO, leading to a better phase stability. Moreover, in this way, the signal is always generated at about the same time delay from the LO and its spectral interference does not change much during the experiments, thus avoiding all the artifacts arising when the signal is moving in time. For example, when the recorded spectral interference is pushed near the limit resolution of the detection system, false decay of the signals can be possibly generated.

It must be recognized, however, that this choice can generate different issues. It indeed implies scanning the first two pulses in different ranges of their associated wedge positions, possibly resulting in different chirp in pulse 1 and 2 for each population time t_2 . This complication can be overcome through a careful use of the pulse shaper that can be suitably tuned so to recompress the pulses at every t_2 delay (Section 3). Furthermore, if the phase difference between the third interaction and the LO

is kept fixed, then the phase stability depends critically only on the phase difference between the first two interactions. It is thus necessary to achieve a strict control over the t_1 delay (and also t_2 for 2Q signals) and therefore particularly reliable wedge calibration procedures have been set up (Section 4).

Once the wanted time ordering is set, the four beams are focused onto the sample by DSM2 with a focal length of 200 mm. The third-order signal propagates in the LO direction and their ensuing interference is delivered to the spectrograph (Andor Shamrock 303i) equipped with a CCD camera (Andor Newton 920) for detection. The CCD is calibrated exploiting the capability of the AOPDF to produce holes in the pulse spectrum. The AOPDF is calibrated using certified absorptive filters (holmium oxide solution and didymium glass from Hellma).

During the 2DES experiment, the CCD camera collects other spurious contributions besides the signals. A suitable acquisition method and a post-processing procedure are thus necessary to remove the unwanted contributions and gain a high signal-to-noise ratio. The acquisition methodology is based on the double modulation lock-in method proposed by Augulis and Zigmantas [21] and will be discussed in detail in Section 5.

3. COMPRESSION AND SHAPING STAGE

The pulse properties are determined by two factors: the shape of the laser spectrum and the phases of its spectral components. The shape of the laser spectrum affects the shape of the final 2DES maps [22,23] while a distortion of the phase (like in chirped pulses) leads to longer pulse duration, reducing the resolution of the experiment [12], and to altered 2DES maps [24,25]. Therefore, it is necessary to work with transform-limited (TL) pulses, defined as the shortest possible pulses for a given optical laser spectrum, to obtain high-quality 2DES data. This condition is achieved when the phase $\phi(\omega)$ is a linear function of the frequency ω [26]. Possible non-linear deviations of the phase, mainly caused by propagation in transmissive optics, have to be compensated to retrieve the TL (and thus temporally compressed) pulse at the sample position. In the implemented setup, this is performed by a pulse-shaping stage consisting of an AOPDF and a prism compressor [27,28], used to relieve the self-induced chirp of the Dazzler crystal.

The AOPDF employs a Taylor expansion of the phase of the electric field around the central frequency of the pulse spectrum, ω_0 . The terms of the expansion at different orders describe different properties of the temporal profile of the pulse. The linear term is related to the arrival time of the pulse, while the second order describes the linear chirp. Higher even (odd) terms correspond to phase distortions with point (axial) symmetry with respect to ω_0 [29].

The measurement of the pulse profile is performed with the frequency-resolved optical gating (FROG) technique at the sample position [30] that reveals the frequency-resolved auto-correlation of the pulse. In our setup, we can take advantage of the BOXCAR geometry to perform FROG by replacing the sample with a non-zero third-order material, typically a solvent. The use of the same cuvette in the same position for sample and solvent guarantees identical operating conditions in

FROG and 2DES measurements, keeping the same pulse properties in the two experiments. The procedure to recover a TL pulse consists of manually modifying the coefficients of the expansion *via* the AOPDF and checking the FROG result until the best conditions are found.

In the experiment the delay times are set modulating the thickness of the wedge medium traversed by the beams. This implies that, at different time delays, the pulses can be affected by different chirp and thus the optimal compression conditions are position dependent. Therefore we must evaluate if and when the chirp is negligible or how we can correct its impact on the final signal. This issue is particularly relevant in the t_2 scan during R and NR experiments, where the full thickness of the wedges is exploited. The chirp has two main effects: a decrease of the maximum signal intensity and the presence of distortions because the medium dispersion leads to frequency-dependent time delays.

Simulation of FROG time traces [29] can be used to predict the loss of heterodyne third-order signal as a consequence of the chirping of the pulses. This procedure is applied to monitor in particular how the maximum intensity of the simulated FROG decays as a function of the chirp induced during the t_2 scan. The pulse duration, specified as full width at half-maximum (FWHM), must be accounted for in the discussion; indeed the shorter the pulse duration, the larger the bandwidth of the laser spectrum and the bigger the effect of the dispersion. The contour plots in Fig. 2 report the ratio between the maximum of the FROG traces simulated with chirped pulses and FROG traces simulated with optimal TL pulses, as a function of the pulse duration and the imposed delay. Deviations from the ideal fully compressed condition are studied as function of wedge material [panel (a)], different pulse shaping operating parameters [panel (b)], and different pulse spectrum central frequency [panel (c)]. It is clear that the greatest aberrations are expected for short pulses at long time delays. Therefore, the capability to manage large bandwidth, and thus short pulses, sets the limit of the maximum delay that can be investigated

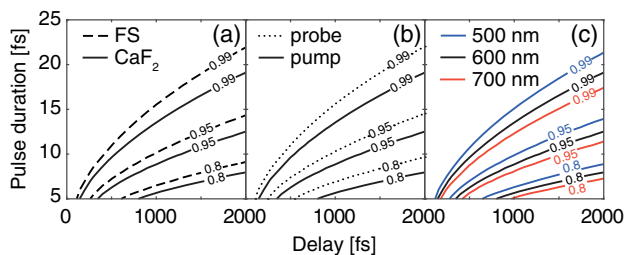


Fig. 2. Contour plots showing the ratio between the maximum intensity of the FROG traces simulated with chirped pulses and with optimal TL pulses. The results are plotted as a function of the pulse duration (x -axis) and t_2 delay (y -axis). In the simulations the chirp reproduces the experimental conditions. The pump pulses E_1 and E_2 are considered identical and fixed in time, whereas the probe pulse E_3 pulse is moved in time. Comparison between the loss of FROG intensity induced by (a) the chirp in CaF_2 and fused silica (FS) wedges; (b) the chirp in CaF_2 wedges when the AOPDF is set to optimize the compression of the probe pulse (dotted line) or of the pump pulses (solid line); (c) considering different central wavelengths of the pulses, employing CaF_2 wedges and compressing the pump pulses.

with a negligible loss of signal. In this context the use of CaF_2 wedges allows to reliably scan a time interval about 30% longer than fused silica wedges [Fig. 2(a)]. Moreover the capability of managing a specific bandwidth depends sensibly upon the central wavelength of the pulse spectrum [Fig. 2(c)]. The same simulations can also be used to find the best operating conditions of the pulse shaper at each investigated t_2 value. In our setup the AOPDF is indeed programmable to minimize the chirp effect at each t_2 . Since the AOPDF is positioned before the DO, it affects in the same way all the pulses. Thus it cannot operate independently on the different pulses of the experimental sequence and the optimal TL conditions for pump pulses (E_1 and E_2) do not necessarily correspond to optimal conditions for the probe (E_3) pulse. The simulations in Fig. 2(b) confirm that the best choice is to set the pulse shaper apparatus so to maximize the pulse compression of the pump pulses at each t_2 . The Sellmeier expression of CaF_2 refractive index [31] is used to obtain the expansion coefficient to program the AOPDF. The choice of programming the AOPDF to keep compressed the pump pulses with respect to the probe pulse allows for another gain of about 30% in the exploitable time interval, see Fig. 2(b). The effect of the medium-induced chirp and how it can be effectively corrected through a smart programming of the AOPDF is illustrated in Fig. 3, reporting an example of FROG measurement recorded at different wedge positions.

The procedure described above is able to correct and minimize the loss of signal due to the chirp but it leaves unmodified the frequency-dependent timing distortions due to the dispersion induced by the wedges. It follows that the higher-frequency components are subjected to a longer delay than the lower-frequency components, resulting in a frequency shift after Fourier transforming from the time to the frequency domain. This leads to possible distortions of the signal along the excitation axis in 2DES maps and frequency shifts of the coherence beating detected along the t_2 axis. In order to estimate and possibly correct these aberrations, the time delay imposed through wedge motion can be expressed as a function of the frequency:

$$t(\omega) = \left(1 + \frac{n_{\text{CaF}_2}(\omega) - n_{\text{air}}(\omega)}{n_{\text{CaF}_2}(\omega_0) - n_{\text{air}}(\omega_0)} \right) t(\omega_0), \quad (1)$$

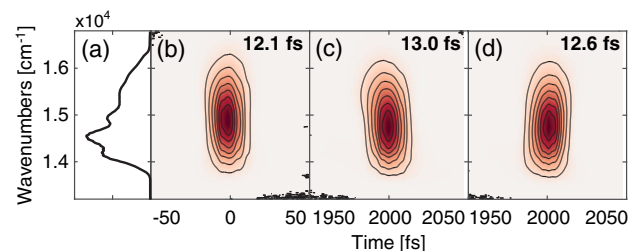


Fig. 3. (a) Laser spectrum used in ZnPc measurements. (b) Pulse profile measured by FROG experiment at optimal TL conditions. (c) FROG experiment in the same conditions but measured at extreme positions of the wedges delay ($t_2 = 2$ ps), showing a slight chirp. (d) FROG experiment at $t_2 = 2$ ps after the phase correction of the Dazzler that retrieves the compressed condition.

where n_{CaF_2} and n_{air} are the refractive indices of CaF_2 and air, respectively and $t(\omega_0)$ is the time delay determined for the central frequency of the laser spectrum. The pulse chirp can be estimated using the group velocity dispersion of the medium, the thickness of the interposed material and the bandwidth taken as FWHM. Equation (1) can be used to evaluate the timing distortions due to the dispersion and to correct them, if needed, during the signal processing operations. For example, for a TL laser pulse centered at 600 nm and with 15 fs pulse duration, a chirp of 10 fs is estimated when a 2000 fs time delay is imposed by CaF_2 wedges, corresponding to a timing error of 0.5% at the wedges extreme positions.

4. TIME DELAYS CALIBRATION

A crucial step in setting a 2DES experiment is the calibration of translation stages that regulate the wedge positions and the amount of CaF_2 that the pulse passes through. A sub-femtosecond precision of the time delay within the entire scanned range is necessary to achieve a full control over the phases of the pulses and therefore obtain a meaningful 2DES map. In a non-collinear 2DES measurement the phase of the signal depends indeed on the phase of all pulses. When the time delay is controlled by a translation stage, its accuracy should be adequate to conserve the phase difference between pulses. The methodology for time delay calibration here proposed is based on the determination of the sub-cycle time delays from the local oscillator [17].

The starting point is the definition of a linear relation that associates the position x_i [in millimeters (mm)] of the i th linear stage, and thus the position of the optical wedge, to a time delay τ_i [in femtoseconds (fs)] of the i th pulse: $\tau_i = c_i(x_i - z_i)$, where c_i is the linear calibration coefficient (fs/mm) that has to be determined and z_i (mm) are the zero time positions at which all the pulses have the same time delay from the LO. The LO is taken naturally as a reference because it is the only pulse whose timing (τ_{LO}) is fixed since it is not controlled by a WP.

The procedure of time delay calibration consists of three main tasks: (i) determining time zero of the experiment and therefore the positions z_i of the three linear stages that satisfy the equation $\tau_i(z_i) = 0$ fs; (ii) finding the linear coefficients c_i to convert a displacement of the stage in a time delay from the zero of the experiment; and (iii) finding the precise value of τ_{LO} .

The typically employed calibration procedure consists of recording the spectral interference (SI) produced by two pulses [32,33]. To this purpose, a 25 μm pinhole is placed where the four beams are focused at the sample position and the SI is recorded by the spectrometer. The Fourier transform of the SI is the simplest method to correlate the position of the stages with the time delay between the LO and the selected pulse: when a spectral interference between two pulses is Fourier transformed, a peak in the time domain is obtained, which is centered at the delay time between the interfering pulses. As this delay increases, the number of fringes in the resulting SI increases shifting the peak in the time domain at longer times. This method works only until the CCD camera and the spectrograph can spectrally separate the fringes of the

interference; therefore, it could fail at long values of delay times such as 2 ps.

Moreover, the adopted pulse sequence with the third interaction fixed and phased-locked with the LO, makes particularly crucial a full control over the relative time and phase of the first two pulses. Therefore, a new procedure has been proposed to fulfill these requirements. With respect to previously proposed approaches [33,34] where each wedge is calibrated independently, our method allows a more robust determination of time-zero positions thanks to the delay correlations plots \mathbf{H} , that correlate the positions of *couples* of stages (Section 4.A). Moreover, a further step of refinement of the linear calibration coefficients has been added, ensuring a reliable phase-locking condition between the first two pulses, effectively scanned in our experimental configuration (Section 4.B).

The first step consists of estimating a set of positions $x_{i,\text{in}}$ of the three stages that roughly induce the same delay from the LO. This evaluation can be performed by adjusting the stages in order to produce similar interference patterns. We subsequently scan each stage x_i in a short range, about 20% of the length of the wedges, around $x_{i,\text{in}}$ and obtain three matrices $\mathbf{F}^{(i)}$ of spectral interferograms, recorded for different positions x_i and resolved in frequency ω by the spectrograph [see Fig. 4(a)]. Every column of the matrix $\mathbf{F}^{(i)}$ represents an interference spectrum, which evolves as the delay between the interfering beams changes due to the motion of the linear stage. At this point we have three matrices, $\mathbf{F}^{(1)}$, $\mathbf{F}^{(2)}$, and $\mathbf{F}^{(3)}$, that contain all the information about the evolution of the pulse delays with respect to the fixed LO as the stages move.

A. Evaluation of Zero Positions

The procedure is based on differences of interference spectra. One of the exciting beams, for example E_1 , is selected as the reference pulse. One at a time, the remaining two beams are compared with the reference. Here the procedure is illustrated for beam E_2 , but the same will be applied for beam E_3 . The main objective of this processing is to produce, from the interference patterns $\mathbf{F}^{(1)}$ and $\mathbf{F}^{(2)}$, a delay correlation plot called $\mathbf{H}^{(2)}$, which correlates the positions of the two stages, showing a clear signature when the two pulses are synchronous. The elements of matrix $\mathbf{H}^{(2)}$ are defined as

$$H_{kl}^{(2)} = \text{envelope} \left(\sum_j |F_{jk}^{(2)} - F_{jl}^{(1)}| \right), \quad (2)$$

where the index j runs over the frequency axis and the indices k and l run over the positions of the stages x_2 and x_1 , respectively. For a specific l value, the data matrix with elements $F_{jk}^{(2)} - F_{jl}^{(1)}$ is retrieved. This matrix presents a characteristic checkerboard pattern, as shown in Fig. 4(b). The absolute value of this matrix is spectrally integrated, obtaining an oscillating function of x_2 [solid black line in Fig. 4(c)]. This oscillatory trace has its biggest amplitude in the correspondence of the position of the stage x_2 that assures an equal delay for the compared pulses. The envelope of this oscillating curve is computed subtracting the constant part and taking the absolute value of the analytic signal [35], obtaining the dashed black line in Fig. 4(c). The matrix $\mathbf{H}^{(2)}$ is then built collecting all the envelopes derived from all the possible l indices [Fig. 4(d)]. A linear function

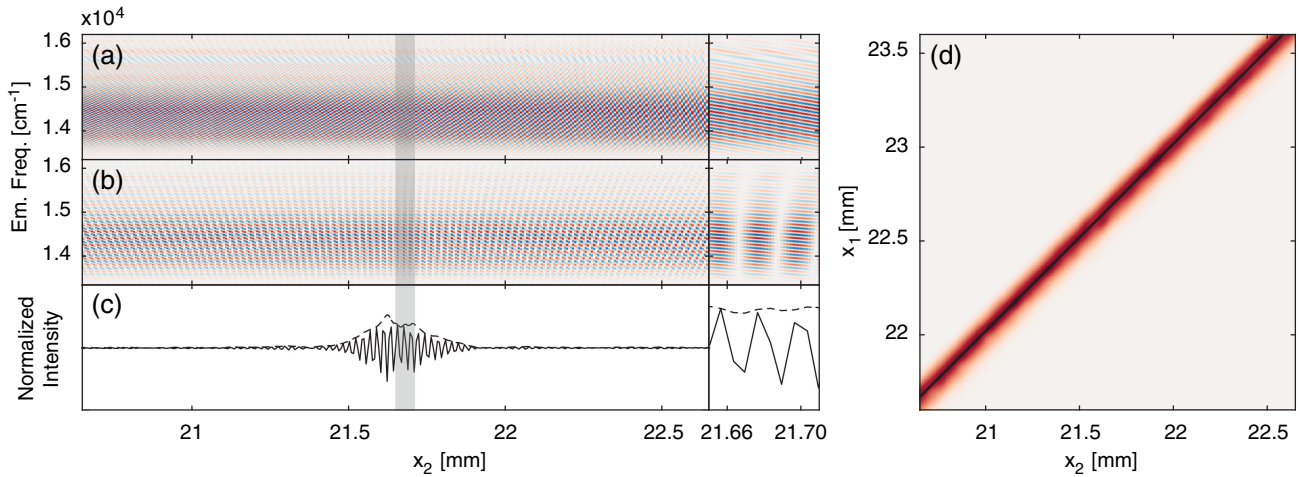


Fig. 4. Procedure for the evaluation of the zero positions of the stages exemplified for E_2 with E_1 taken as reference. (a) Graphical representation of the matrix $\mathbf{F}^{(2)}$; (b) matrix with elements $F_{jk}^{(2)} - F_{jl}^{(1)}$ with $F_{jl}^{(1)}$ taken at $x_{1,l} = 22.65$ mm; (c) the solid line is the result of the integration of the absolute value of the matrix in panel (b) along the frequency dimension, the dashed line is the envelope computed with the analytic signal. The insets on the right of panels (a)–(c) show enlargements of the traces in a limited interval of x_2 (grey area). (d) Matrix $\mathbf{H}^{(2)}$ showing a clear signature only at the (x_1, x_2) coordinates where the pulses are synchronous. The black line represents the linear fit performed with Eqs. (4) and (5).

can be used to fit the trend observed in matrix $\mathbf{H}^{(2)}$. The function is defined as

$$z_2(x_1) = mx_1 + q, \quad (3)$$

where m and q are the slope and the intercept of the linear function. Each point on the line can be used as actual zero position of the calibration. In other words, with this linear function we can choose an arbitrary position as zero for the reference stage and automatically get the zero position for the other stages. In order to practically and reliably obtain the parameters m and q of the linear function, we can fit matrix $\mathbf{H}^{(2)}$ with a Gaussian surface represented in the matrix \mathbf{G} . The center of the Gaussian function is modeled with the linear function in Eq. (3) obtaining a Gaussian tunnel shape. The matrix elements of \mathbf{G} are defined as

$$G_{lk}(a, b, m, q) = ae^{-\left(\frac{x_{2,k} - z_2(x_{1,l})}{b}\right)^2} = ae^{-\left(\frac{x_{2,k} - (mx_{1,l} + q)}{b}\right)^2}, \quad (4)$$

where a is a scaling factor, b is the width of the Gaussian function, and the indices k and l are associated with the k -th and l -th positions $x_{2,k}$ and $x_{1,l}$, respectively. Then the following unconstrained least-square minimization problem is solved:

$$\min_{(a,b,m,q) \in \mathbb{R}^4} \|\mathbf{H}^{(2)} - \mathbf{G}(a, b, m, q)\|^2, \quad (5)$$

given a good set of starting parameters the Gaussian surface is rapidly fitted. The same procedure is repeated for the third pulse, so that for any arbitrary choice of z_1 , the zero stage positions z_2 and z_3 , in which the three exciting pulses are contemporary, are determined. This condition is used as the time-zero of the experiment.

B. Evaluation of the Calibration Coefficients

The second part of the calibration procedure consists of determining the linear coefficients c_1 , c_2 , and c_3 that allow accurately moving the pulses from the zero positions. The optimal procedure should provide conversion coefficients able to guarantee,

at the maximum excursion of the linear stages, a time error much smaller than the optical cycle of the electromagnetic radiation. This accuracy assures that the final signal, recorded during experiments, is correctly phase-locked. The idea at the basis of this procedure is to mathematically compensate for the evolution of the spectral interference coupled to the movement of the wedge. In other words, we want to determine which is the exact delay to be mathematically subtracted in order to achieve a perfectly constant interference pattern. We will describe the procedure for the pulse E_1 ; the same applies for the other pulses.

First, matrix $\mathbf{F}^{(1)}$ is Hilbert transformed along the frequency axis in order to operate on the complex analytic signal. This allows subtracting the delay $\tau_1(x_1) = c_1(x_1 - z_1)$ from the spectral interference multiplying by an oscillating exponential function as

$$L_{jk}^{(1)}(c_1) = F_{jk}^{(1)} e^{-i\omega_j c_1 (x_{1,k} - z_1)}, \quad (6)$$

where for the correct c_1 value the matrix $\mathbf{L}^{(1)}$ is a collection of constant interference spectra. This operation cancels out the time delay τ_1 induced by moving the WP from the zero position z_1 . In order to retrieve the exact parameter c_1 , we can solve a maximization problem for an objective scalar function which exploits the condition of the constant interference pattern that we want to achieve. The problem is defined as

$$\max_{c_1 \in \mathbb{R}} \sum_j \left| \sum_k L_{jk}^{(1)}(c_1) \right|, \quad (7)$$

where the first summation over the index k , which runs over the stage positions, is going to output non-null values only if there are no oscillations along that direction. The summation over j serves to obtain the final scalar objective function of the maximization. All the parameters c_i are then recovered repeating the procedure for the three stages.

The interference spectra in matrices $\mathbf{F}^{(i)}$ used for the previous calculation are sampled only within a limited portion of the stage movement range. This is because at large delay values the spectrometer is not able to efficiently resolve all the fringes of the SI. This is not detrimental for the accurate evaluation of the zero positions of the stages but it may generate inaccuracy at the extreme positions of the stages. This is particularly critical for pulses E_1 and E_2 , whose position in time is effectively scanned during the experiment, exploiting the full length of the optical wedges. The third pulse and LO are instead fixed during R and NR measurements, and are not delayed relevantly in 2Q experiments. Therefore, we verify that the relative phase between E_1 and E_2 is conserved also at the extreme positions and possible small errors, even of fractions of an optical cycle, are corrected.

In practice, using the calibration coefficients previously determined, x_1 and x_2 are moved simultaneously so to keep $\tau_2 - \tau_1$ constant. The interference pattern generated by interaction of E_1 and E_2 as a function of the position x_1 (or x_2) and ω is recorded and the matrix $\mathbf{F}^{(1,2)}$ is retrieved. If the spectral interference is constant for the full scanned range, then the calibration is accurate and ready for the experiments. When a small linear drift of the phase of the interference is observed, it means that the values of the linear coefficients are not fully rigorous in the whole range and they must be corrected to avoid phase drift of the third-order signal.

To this purpose, it is possible to define a corrected interference pattern as

$$L_{jk}^{(1,2)}(p) = F_{jk}^{(1,2)} e^{-i\omega_j(p\tau_{1,k})}, \quad (8)$$

where $p\tau_{1,k}$ is the small delay correction to be applied, and p is an adimensional scaling parameter. Analogously to problem (7) we can maximize a scalar function solving the following problem:

$$\max_{p \in \mathbb{R}} \sum_j \left| \sum_k L_{jk}^{(1,2)}(p) \right|. \quad (9)$$

The phase drift is caused by an error in the relative time positions $\tau_2 - \tau_1$ and not in the absolute time positions of the two pulses. Assuming that the correction is small, it is convenient to include the whole corrective factor only in the calibration coefficient of one of the two pulses, e.g., we can take c_1 as exact and impose the correction factor only on c_2 . In these conditions, it can be demonstrated that the corrected coefficient $c_{2,\text{corr}}$ can be expressed by

$$c_{2,\text{corr}} = c_2(p + 1). \quad (10)$$

This correction is usually smaller than the 0.05%, but it is fundamental for removing any phase trend of the third-order signal induced by calibration uncertainty. Figure 5 compares 2DES maps at three different population times t_2 , obtained with [Figs. 5(d)–5(f)] and without [Figs. 5(a)–5(c)] the linear correction of the calibration coefficients. A clear spurious phase trend is introduced for long t_2 values if the correction in Eq. (10) is not accounted for. We verified that in our setup the phase drift has a predominant linear trend as a function of the positions. After the correction described in Eq. (10) we retrieved the trend shown in Fig. 5(g) that demonstrates that the

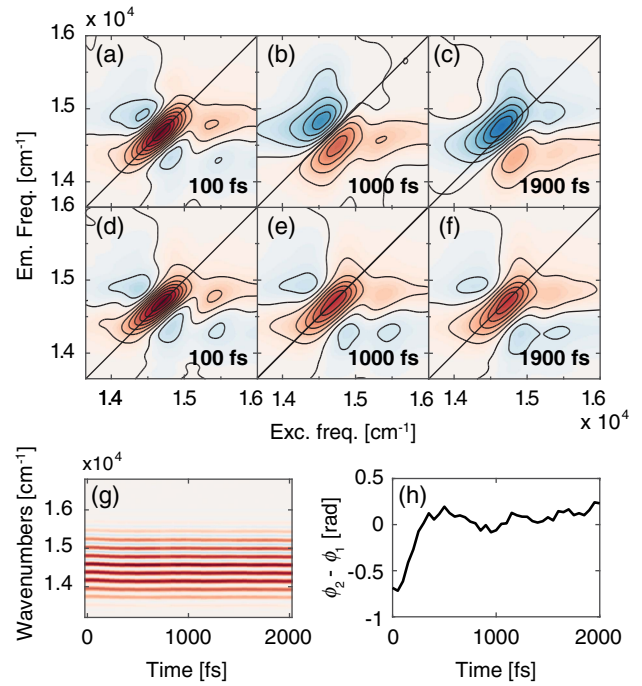


Fig. 5. Distortions of rephasing 2DES maps arising when effects of phase drift at extreme positions of the delay lines are not accounted for. (a)–(c) 2DES maps obtained using the calibration coefficients before linear drift correction. (d)–(f) The same 2DES maps determined using the calibration coefficients corrected as in Eq. (10). Measures performed on a THF solution of ZnPc. (g) SI of E_1 and E_2 with $t_1 = 150$ fs scanned over the entire wedge applying correction in Eq. (10). (h) Phase error between E_1 and E_2 after the correction.

linear trend is indeed well suited. However, manufacturers produce high but not absolute precision wedges. Indeed, Fig. 5(h) shows that, after the correction of the linear coefficient in Eq. (10), small phase deviations are still present and have to be corrected during data processing.

C. Evaluation of the Delay from the LO

The last step consists of retrieving the precise value of τ_{LO} . This task cannot be accomplished by simply looking at the SI generated by the $25 \mu\text{m}$ pinhole used for the calibration, because this configuration does not reproduce conveniently the exact working conditions of 2DES experiments. We therefore suggest to exploit the heterodyne non-resonant FROG of a solvent in a cell at the sample position. The procedure consists of collecting the interference patterns produced by the LO and the third-order non-resonant signal of the solvent generated when all the pulses are superimposed in time. During this experiment, all the stages positions x_i are scanned simultaneously around their z_i values, so to keep $\tau_{\text{FROG}} = \tau_1 = \tau_2 = \tau_3$. Therefore, we obtain a matrix of interference patterns which evolves as a function of $\tau_{\text{LO}} - \tau_{\text{FROG}}$, similar to matrices $\mathbf{F}^{(i)}$. This matrix is Fourier transformed along the frequency axis obtaining a new matrix, which has a tunnel-like shape similar to matrix $\mathbf{H}^{(2)}$. A minimization procedure analogous to the one reported in Eq. (5) can be applied and a more accurate value of τ_{LO} at $\tau_{\text{FROG}} = 0$ fs can be extrapolated.

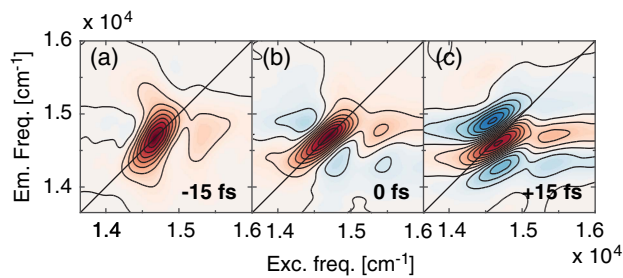


Fig. 6. Distortions of a rephasing 2DES map caused by an inaccurate determination of τ_{LO} . Panels (a), (b), and (c) show errors of -15, 0, and +15 fs in retrieving a $\tau_{LO} = 489$ fs, respectively. The measure was performed on a THF solution of ZnPc at $t_2 = 100$ fs.

The determination of the exact value of τ_{LO} is a crucial parameter in the processing of the 2DES spectrum (see the next section). The time distance of the LO from the zero of the experiment (τ_{LO}) controls indeed how dense the fringes of the interference pattern in the collected spectra are, usually is set at about 400 fs. As an example, Fig. 6 shows the effects of an error in the estimation of τ_{LO} in the final 2DES rephasing map.

5. DATA ACQUISITION AND PROCESSING

A double lock-in modulation acquisition [21] is implemented in order to suppress the spurious contributions in the recorded spectra. In this acquisition procedure, E_2 and E_3 exciting pulses are modulated by two phase-locked optical choppers at two different frequencies, ν_{E_2} and ν_{E_3} , in order to isolate the signal from almost all the other contributions after a Fourier transform operation. The laser pulse train, the CCD camera, and the optical choppers are reciprocally triggered and phase-locked. To fully exploit the potential of this method, each modulation frequency must be carefully chosen. First, the signal should be extracted at a frequency ν_S lower than the Nyquist limit, so that $\nu_S < \nu_{CCD}/2$, with ν_{CCD} being the sampling frequency of the detector. Second, to avoid phase instability it is convenient to set the higher modulating frequency as a multiple of the lower one. However, since the choppers modulate the beams with square waves, the scattering contributions modulated at

the lower frequency are distributed in all their odd harmonic frequencies. Therefore, taking the higher frequency as the odd multiple of the lower one is a convenient approach, since it guarantees that the modulation frequencies of the signal are always even multiples of the slower modulation. The signal can be eventually retrieved at both sum and difference frequencies, $\nu_S^+ = \nu_{E_2} + \nu_{E_3}$ and $\nu_S^- = \nu_{E_2} - \nu_{E_3}$, respectively. The signal is recovered as the real part of the Fourier transform of the series of spectra acquired by the detector. There is a particular combination of relative phases between the two modulations and the CCD sampling for which the real part of the signal is maximized at both sum and difference frequencies and the maximum signal-to-noise ratio can be achieved. In our setup, $\nu_{CCD} = 500$ Hz, $\nu_{E_2} = 200$ Hz, and $\nu_{E_3} = 40$ Hz; thus the signal can be extracted at $\nu_S^- = 160$ or $\nu_S^+ = 240$ Hz or both. With this method, most of the scattering contributions are removed, since they reach the CCD camera with the frequency of modulation of a single chopper or they are not modulated at all.

However, the acquired signal still contains the unwanted homodyne third-order signal, $|E_S|^2$, the spurious contribution arising from the interference between the signal and the scattering of the non-modulated beam, $E_S E_1^*$, and the interference between the scattering of the modulated beams, $E_3 E_2^*$, so that the raw signal acquired by the CCD can be expressed as $S^{(a)}(t_1, t_2, \omega_3) = |E_S|^2 + 2\Re\{E_S E_{LO}^*\} + 2\Re\{E_S E_1^*\} + 2\Re\{E_3 E_2^*\}$. An example of rephasing data collected at a fixed population time is reported in Fig. 7(a).

First, to isolate the pure signal E_S from the contribution $E_S E_{LO}^*$, it is necessary to enforce the time ordering between the signal and the local oscillator. The recorded interference can be expressed as $E_S E_{LO}^* = \mathcal{E}_S(\omega_3) \mathcal{E}_{LO}(\omega_3) e^{i\omega_3(\tau_S - \tau_{LO})}$, where $\mathcal{E}_S(\omega_3)$ and $\mathcal{E}_{LO}(\omega_3)$ are the square root of the spectra of the corresponding fields. The local oscillator arrives at the CCD after the signal, thus we need to impose that $\tau_S - \tau_{LO}$ is negative. This operation is performed (i) by inverse-Fourier transforming $S^{(a)}$ along ω_3 , (ii) by retaining only the negative part of the resulting time axis, and (iii) by Fourier transforming back. After this set of operations, the signal $S^{(a)}$ becomes a complex valued signal $\hat{S}^{(a)}$: the real part is equal to the data recorded by the CCD and the imaginary

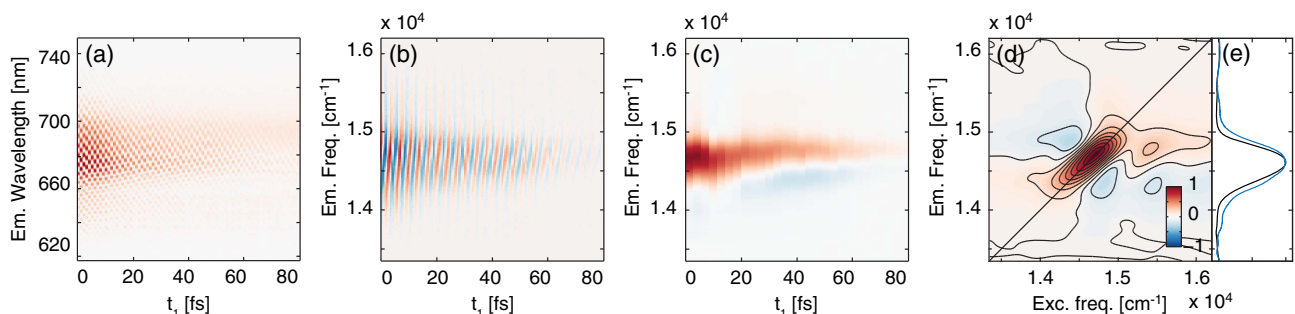


Fig. 7. Step-by-step description of the implemented data processing procedure. (a) Raw signal $S^{(a)}$ acquired for a rephasing experiment at a fixed value of t_2 ; (b) signal $S^{(b)}$ is retrieved after applying the correction for the delay from LO; (c) signal $S^{(c)}$ is obtained after the application of the rotating frame approach and the application of a window filter in the t_3 domain to remove residual spurious contributions; (d) final 2DES map obtained after Fourier transform along t_1 , shift from the reference frequency and phase correction. (e) Comparison between pump-probe spectrum (blue line) and projection onto emission axis of the total 2DES spectrum (black line). The measure was performed on a THF solution of ZnPc at $t_2 = 100$ fs.

part is a copy of the original data with a phase shift of $-\pi/2$. The delay τ_{LO} can now be added and at the same time the data are divided by the square root of the LO spectrum giving

$$S^{(b)} = \hat{S}^{(a)} e^{i\omega_3\tau_{LO}} / \mathcal{E}_{LO}(\omega_3), \quad (11)$$

as reported in Fig. 7(b). Equation (11) highlights how an accurate estimation of τ_{LO} is crucial to retrieve artifacts-free 2D maps, as already discussed in Section 4.C.

At this point a rotating frame (RF) can be applied, as previously suggested by Schlaw-Cohen *et al.* [36]. For R and NR signals, this is done detuning the optical frequency during t_1 by subtracting a reference frequency ω_{ref} , which is usually taken as the central frequency of the laser bandwidth:

$$S_R^{(c)} = S_R^{(b)} e^{i\omega_{ref}t_1}, \quad (12)$$

$$S_{NR}^{(c)} = S_{NR}^{(b)} e^{-i\omega_{ref}t_1}. \quad (13)$$

After this operation, the resulting R and NR signals, $S_R^{(c)}$ [Fig. 7(c)] and $S_{NR}^{(c)}$, respectively, retain only slow modulations along the coherence time t_1 . It follows that their sampling frequency in t_1 can be greatly reduced. The maximum frequency observed in the RF signal corresponds to half of the bandwidth of the laser spectrum, which is of the order of few thousands of cm^{-1} . Note that the RF is introduced here *a posteriori* after the data acquisition and only at the level of data processing calculation. The procedure does not require specific pulse scan schemes, leading to maximum freedom and flexibility in the control of pulse timings. This post-processing approach allows acquiring and managing undersampled data, greatly reducing the acquisition time. It does not improve the quality of the data but speeds up the acquisition of a single map that can be anyway averaged in case of a low signal-to-noise ratio. Note that the undersampling of 2Q signals is not necessary because the final response is a single map and therefore the acquisition time is already very fast [37].

In order to remove the remaining spurious contributions from the signal, a time-filtering in the t_3 dimension is applied using a super-Gaussian function. The filter is tuned to keep only the portion of the t_3 axis between zero and about 100–150 fs, after which the signal is completely decayed. This operation removes most of the remaining spurious contributions in the recorded signal, including the homodyne third-order signal, because the operation in Eq. (11) shifts all these contributions by τ_{LO} and thus outside the filter window. The initial transient of the signal can be slightly affected by $E_3E_1^*$ and $E_3E_2^*$ when the delay between signal and E_1 and the delay between E_3 and E_2 are inside the filter window, respectively. This condition is verified only at early values of population time and does not arise any concern for the rest of the data.

The small dispersion of the pulse spectral components affecting t_1 and t_2 delays is corrected applying Eq. (1) and interpolating the new data. This step of data processing is necessarily performed after the RF because the interpolation of the t_1 axis is not feasible when dealing with undersampled data.

The next step is the Fourier transform along t_1 (or t_2 in the case of 2Q maps), to obtain the final frequency-frequency maps. The resulting excitation frequency axis ω_1 must then be shifted by ω_{ref} to account for the rotating frame previously applied. Finally, the arbitrary phase of the signal with respect to

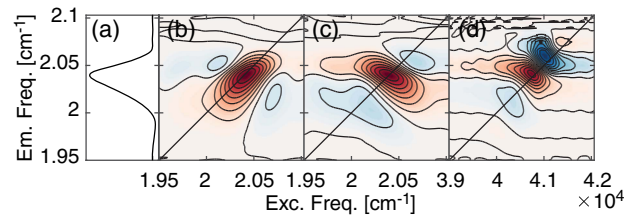


Fig. 8. Examples of the different responses achievable with the described setup suitably modifying the pulse sequence: (a) pump-probe spectrum; (b) rephasing and (c) non-rephasing 2DES maps at a fixed t_2 value (100 fs); (d) 2Q map. The measures were performed on aqueous solutions of H_2TPPS J-aggregates at room temperature.

the LO must be removed to isolate the real from the imaginary part. As suggested in [2], this last step is performed exploiting the projection-slice theorem. The same phase shift is employed for the phasing of R, NR, and 2Q signals, as long as these measurements are performed with the same calibration conditions.

At this point, the processed signal and its time evolution along t_2 is ready to be examined with the various data analysis procedures proposed to extract information about populations and coherent dynamics [38–48]. The versatility of this setup is exemplified in Fig. 8 that reports the pump-probe spectrum, the R and NR maps recorded at $t_2 = 100$ fs, and the 2Q map for a solution of J-aggregates of H_2TPPS . This particular system represents an ideal example of how the synergic use of high-quality R, NR, and 2Q response can provide a clear picture of very subtle details of the excitonic structure and dephasing mechanisms in complex systems, not accessible by single measurements [5].

6. CONCLUSIONS

We reported a detailed description of a versatile fully non-collinear setup for 2DES spectroscopy. Novel implementations in the optical layout and in calibration and data processing procedures have been proposed to efficiently obtain high-quality and artifacts-free 2DES spectra along different phase-matching directions. With respect to previously proposed fully non-collinear wedge-based setups, we introduced the use of 4° wedge pairs, allowing longer scanning times (up to 2 ps). The particular optical layout of the setup allows an independent control the three pulse delays, giving access to rephasing, non-rephasing, and double quantum signals simply imposing the correct pulse sequence. Possible aberrations introduced especially at long delay times by the dispersion of the wedge medium have been estimated and discussed. Correction methodologies based on a fine control of the phases of the pulses with an AODPF pulse shaper and a robust wedge calibration procedure have been proposed. Reduced acquisition times were achieved thanks to the application of an *a posteriori* rotating frame approach that allows a drastic reduction of the number of data points along t_1 to acquire a single map.

Funding. H2020 European Research Council (ERC) (QUENTRHEL (278560)); Seventh Framework Programme (FP7) (MULTI (317707), PAPETS (323901)).

REFERENCES

1. E. Collini, "Spectroscopic signatures of quantum-coherent energy transfer," *Chem. Soc. Rev.* **42**, 4932–4947 (2013).
2. D. M. Jonas, "Two-dimensional femtosecond spectroscopy," *Annu. Rev. Phys. Chem.* **54**, 425–463 (2003).
3. A. M. Brańczyk, D. B. Turner, and G. D. Scholes, "Crossing disciplines—a view on two-dimensional optical spectroscopy," *Ann. Phys.* **526**, 31–49 (2014).
4. A. Nemeth, F. Milota, T. Mančal, T. Pullerits, J. Sperling, J. Hauer, H. F. Kauffmann, and N. Christensson, "Double-quantum two-dimensional electronic spectroscopy of a three-level system: experiments and simulations," *J. Chem. Phys.* **133**, 094505 (2010).
5. L. Bolzonello, F. Fassioli, and E. Collini, "Correlated fluctuations and intraband dynamics of J-aggregates revealed by combination of 2DES schemes," *J. Phys. Chem. Lett.* **7**, 4996–5001 (2016).
6. J. D. Hybl, A. W. Albrecht, S. M. Gallagher Faeder, and D. M. Jonas, "Two-dimensional electronic spectroscopy," *Chem. Phys. Lett.* **297**, 307–313 (1998).
7. S.-H. Shim and M. T. Zanni, "How to turn your pump-probe instrument into a multidimensional spectrometer: 2D IR and vis spectroscopies via pulse shaping," *Phys. Chem. Chem. Phys.* **11**, 748–761 (2009).
8. J. A. Myers, K. L. M. Lewis, P. F. Tekavec, and J. P. Ogilvie, "Two-color two-dimensional Fourier transform electronic spectroscopy with a pulse-shaper," *Opt. Express* **16**, 17420–17428 (2008).
9. E. Harel, A. F. Fidler, G. S. Engel, and B. Alexander Pines, "Real-time mapping of electronic structure with single-shot two-dimensional electronic spectroscopy," *Proc. Natl. Acad. Sci. USA.* **107**, 16444–16447 (2010).
10. C. Manzoni, D. Brida, and G. Cerullo, "Phase-locked pulses for two-dimensional spectroscopy by a birefringent delay line," *Opt. Lett.* **37**, 3027–3029 (2012).
11. F. D. Fuller, D. E. Wilcox, and J. P. Ogilvie, "Pulse shaping based two-dimensional electronic spectroscopy in a background free geometry," *Opt. Express* **22**, 1018–1027 (2014).
12. F. D. Fuller and J. P. Ogilvie, "Experimental implementations of two-dimensional Fourier transform electronic spectroscopy," *Annu. Rev. Phys. Chem.* **66**, 667–690 (2015).
13. V. I. Prokhorenko, A. Halpin, and R. J. D. Miller, "Coherently-controlled two-dimensional photon echo electronic spectroscopy," *Opt. Express* **17**, 9764–9779 (2009).
14. A. D. Bristow, D. Karaiskaj, X. Dai, T. Zhang, C. Carlsson, K. R. Hagen, R. Jimenez, and S. T. Cundiff, "A versatile ultrastable platform for optical multidimensional Fourier-transform spectroscopy," *Rev. Sci. Instrum.* **80**, 073108 (2009).
15. M. L. Cowan, J. P. Ogilvie, and R. J. D. Miller, "Two-dimensional spectroscopy using diffractive optics based phased-locked photon echoes," *Chem. Phys. Lett.* **386**, 184–189 (2004).
16. A. Nemeth, J. Sperling, J. Hauer, H. F. Kauffmann, and F. Milota, "Compact phase-stable design for single- and double-quantum two-dimensional electronic spectroscopy," *Opt. Lett.* **34**, 3301–3303 (2009).
17. D. B. Turner, K. E. Wilk, P. M. G. Curmi, and G. D. Scholes, "Comparison of electronic and vibrational coherence measured by two-dimensional electronic spectroscopy," *J. Phys. Chem. Lett.* **2**, 1904–1911 (2011).
18. U. Selig, F. Langhøjer, F. Dimler, T. Löhrlig, C. Schwarz, B. Gieseck, and T. Brixner, "Inherently phase-stable coherent two-dimensional spectroscopy using only conventional optics," *Opt. Lett.* **33**, 2851–2853 (2008).
19. I. A. Heisler, R. Moca, F. V. A. Camargo, and S. R. Meech, "Two-dimensional electronic spectroscopy based on conventional optics and fast dual chopper data acquisition," *Rev. Sci. Instrum.* **85**, 063103 (2014).
20. B. M. Cho, M. K. Yetzbacher, K. Kitney, E. R. Smith, and D. M. Jonas, "Propagation and beam geometry effects on 2D Fourier transform spectra of multi-level systems," *J. Phys. Chem. A* **113**, 13287–13299 (2009).
21. R. Augulis and D. Zigmantas, "Two-dimensional electronic spectroscopy with double modulation lock-in detection: enhancement of sensitivity and noise resistance," *Opt. Express* **19**, 13126–13133 (2011).
22. F. V. de A. Camargo, L. Grimmelsmann, L. Anderson, S. R. Meech, and I. A. Heisler, "Resolving vibrational from electronic coherences in two-dimensional electronic spectroscopy: the role of the laser spectrum," *Phys. Rev. Lett.* **118**, 033001 (2017).
23. V. Perlik, J. Hauer, and F. Šanda, "Finite pulse effects in single and double quantum spectroscopies," *J. Opt. Soc. Am. B* **34**, 430–439 (2017).
24. P. F. Tekavec, J. A. Myers, K. L. M. Lewis, F. D. Fuller, and J. P. Ogilvie, "Effects of chirp on two-dimensional Fourier transform electronic spectra," *Opt. Express* **18**, 11015–11024 (2010).
25. N. Christensson, Y. Avlasevich, A. Yartsev, K. Müllen, T. Pascher, and T. Pullerits, "Weakly chirped pulses in frequency resolved coherent spectroscopy," *J. Chem. Phys.* **132**, 174508 (2010).
26. R. Paschotta, *Encyclopedia of Laser Physics and Technology* (Wiley-VCH, 2008).
27. W. Dietel, J. J. Fontaine, and J.-C. Diels, "Intracavity pulse compression with glass: a new method of generating pulses shorter than 60 fsec," *Opt. Lett.* **8**, 4–6 (1983).
28. R. L. Fork, O. E. Martinez, and J. P. Gordon, "Negative dispersion using pairs of prisms," *Opt. Lett.* **9**, 150–152 (1984).
29. K. W. DeLong, R. Trebino, and D. J. Kane, "Comparison of ultrashort-pulse frequency-resolved-optical-gating traces for three common beam geometries," *J. Opt. Soc. Am. B* **11**, 1595–1608 (1994).
30. D. J. Kane and R. Trebino, "Characterization of arbitrary femtosecond pulses using frequency-resolved optical gating," *IEEE J. Quantum Electron.* **29**, 571–579 (1993).
31. M. Daimon and A. Masumura, "High-accuracy measurements of the refractive index and its temperature coefficient of calcium fluoride in a wide wavelength range from 138 to 2326 nm," *Appl. Opt.* **41**, 5275–5281 (2002).
32. T. Brixner, T. Mančal, I. V. Stiopkin, and G. R. Fleming, "Phase-stabilized two-dimensional electronic spectroscopy," *J. Chem. Phys.* **121**, 4221–4236 (2004).
33. R. Augulis and D. Zigmantas, "Detector and dispersive delay calibration issues in broadband 2D electronic spectroscopy," *J. Opt. Soc. Am. B* **30**, 1770–1774 (2013).
34. D. B. Turner, R. Dinshaw, K.-K. Lee, M. S. Belsley, K. E. Wilk, P. M. G. Curmi, and G. D. Scholes, "Quantitative investigations of quantum coherence for a light-harvesting protein at conditions simulating photosynthesis," *Phys. Chem. Chem. Phys.* **14**, 4857–4874 (2012).
35. S. L. Marple, "Computing the discrete-time "analytic" signal via FFT," *IEEE Trans. Signal Process.* **47**, 2600–2603 (1999).
36. G. S. Schlau-Cohen, A. Ishizaki, and G. R. Fleming, "Two-dimensional electronic spectroscopy and photosynthesis: fundamentals and applications to photosynthetic light-harvesting," *Chem. Phys.* **386**, 1–22 (2011).
37. J. Kim, S. Mukamel, and G. D. Scholes, "Two-dimensional electronic double-quantum coherence spectroscopy," *Acc. Chem. Res.* **42**, 1375–1384 (2009).
38. I. H. M. Van Stokkum, D. S. Larsen, and R. Van Grondelle, "Global and target analysis of time-resolved spectra," *Biochim. Biophys. Acta* **1657**, 82–104 (2004).
39. E. E. Ostroumov, R. M. Mulvaney, J. M. Anna, R. J. Cogdell, and G. D. Scholes, "Energy transfer pathways in light-harvesting complexes of purple bacteria as revealed by global kinetic analysis of two-dimensional transient spectra," *J. Phys. Chem. B* **117**, 11349–11362 (2013).
40. F. V. de A. Camargo, H. L. Anderson, S. R. Meech, and I. A. Heisler, "Time-resolved twisting dynamics in a porphyrin dimer characterized by two-dimensional electronic spectroscopy," *J. Phys. Chem. B* **119**, 14660–14667 (2015).
41. A. Gelzinis, V. Butkus, E. Songaila, R. Augulis, A. Gall, C. Büchel, B. Robert, D. Abramavicius, D. Zigmantas, and L. Valkunas, "Mapping energy transfer channels in fucoxanthin-chlorophyll protein complex," *Biochim. Biophys. Acta* **1847**, 241–247 (2015).
42. J. A. Myers, K. L. M. Lewis, F. D. Fuller, P. F. Tekavec, C. F. Yocum, and J. P. Ogilvie, "Two-dimensional electronic spectroscopy of the D1-D2-cyt b559 photosystem II reaction center complex," *J. Phys. Chem. Lett.* **1**, 2774–2780 (2010).

43. D. B. Turner, K. W. Stone, K. Gundogdu, and K. A. Nelson, "Three-dimensional electronic spectroscopy of excitons in GaAs quantum wells," *J. Chem. Phys.* **131**, 144510 (2009).
44. H. Li, A. D. Bristow, M. E. Siemens, G. Moody, and S. T. Cundiff, "Unraveling quantum pathways using optical 3D Fourier-transform spectroscopy," *Nat. Commun.* **4**, 1390 (2013).
45. J. R. Caram and G. S. Engel, "Extracting dynamics of excitonic coherences in congested spectra of photosynthetic light harvesting antenna complexes," *Faraday Discuss.* **153**, 93–104 (2011).
46. J. Prior, E. Castro, A. W. Chin, J. Almeida, S. F. Huelga, and M. B. Plenio, "Wavelet analysis of molecular dynamics: efficient extraction of time-frequency information in ultrafast optical processes," *J. Chem. Phys.* **139**, 224103 (2013).
47. A. Volpato and E. Collini, "Time-frequency methods for coherent spectroscopy," *Opt. Express* **23**, 20040–20050 (2015).
48. A. Volpato, L. Bolzonello, E. Meneghin, and E. Collini, "Global analysis of coherence and population dynamics in 2D electronic spectroscopy," *Opt. Express* **24**, 24773–24785 (2016).